Invited Paper

Micromachined Fabry-Perot Interferometer with Corrugated Silicon Diaphragm for Fiber Optic Sensing Applications

A. Méndez and T. F. Morse
Laboratory for Lightwave Technology
Brown University, Providence, RI 02912

K. A. Ramsey
Batelle Memorial Institute
Columbus, Ohio 43201-2693

ABSTRACT

A new design for a miniature Fabry-Perot Interferometer (FPI) mounted on the tip of an optical fiber for sensing applications is presented. The Fabry-Perot Cavity (FPC) is formed by a micromachined corrugated silicon diaphragm anodically bonded to a pyrex substrate. In this way, this device takes advantage of the sensitivity and selectivity of an optical interferometer combined with the small size, lightweight and EMI immunity properties of optical fibers to create compact, lightweight and almost entirely dielectric sensors for the measurement of pressure, acceleration, sound, electric and magnetic field, etc. in remote, dangerous or inaccessible places. A discussion on the operation and fabrication of the FPC is given, along with experimental results obtained in its application as an electric field sensor.

INTRODUCTION

Since the reflectivity (or transmissivity) in a FPI is a unique function of the mirror separation, the medium's refractive index, and the wavelength of operation, it is possible to use it as a sensitive and selective transducer for a variety of physical measurands. Thus, by changing the cavity gap by the action of an external agent such as pressure or temperature, while keeping the other parameters constant, it is possible to obtain a shift in the fringe spectrum of the cavity. In the present case, this function is accomplished by a deformable, thin and corrugated silicon diaphragm. Therefore, under the influence of an external measurand, the central portion of said diaphragm (which acts as a cavity mirror) deflects, effectively changing the gap size and with it the intensity of the light reflected or transmitted by the cavity. Furthermore, the use of a corrugated diaphragm has also the advantage of increasing the range of linear deflection, improve the parallelism between the cavity mirrors as well as isolate the cavity from case stresses.

Several FPI utilizing thin Si diaphragms have been described in the past [1-5]. Most of them were used either as narrow band-pass filters for WDM applications in fiber optic systems, or as pressure transducers. Furthermore, fiber optic sensors based on modulating the backreflected light coming from a FPI attached to them have been investigated [6]. Sensors for the measurement of pressure [7-9], temperature [10] and refractive index [11] have been successfully developed.

 0-8194-0972-3/93/$4.00

There are two basic types of operation for these sensors depending on the size of the cavity gap [12]. Large-cavity sensors ($> 5\mu m$) have a multi-cycle operation and thus rely on fringe counting techniques for the determination of the measurand. And short-cavity sensors ($< 5\ \mu m$) having a spectral width comparable to a single fringe. Thus, any shifts of the resonance peak can be directly related to the magnitude of the parameter of interest. Obviously, the former type experience large mirror separations of the order of several μm, while the latter require displacements of less than a μm. The FPC used in this work is of the shallow-cavity type because its compatibility with a simpler detection scheme as opposed to the cumbersome and ambiguous fringe counting circuits associated with a large-cavity FPI.

Fig. 1 depicts the Fabry-Perot cavity (FPC) design. The cavity is formed by a suspended, thin and corrugated silicon diaphragm bonded to a glass substrate. A metallic film on the surface of the silicon diaphragm acts as one of the cavity mirrors, while a thin, partially transmitting, aluminum film on the substrate constitutes the other. The structure is mounted on the tip of a 100/140 μm multimode optical fiber onto which a GRIN lens has been previously attached (see Fig. 2).

The operation of a fiber sensor using one such FPI is very simple. As the gap separation in the cavity changes under the influence of the measurand, the intensity of the backreflected light into the fiber changes accordingly. The spectral shift of the interferometer peak can be interrogated using an LED which translates the cavity's shifts into intensity variations of the LED light spectrum, thus yielding a spectrally modulated envelope. To make the sensor immune to variations in light intensity due to bending or transmission losses, as well as any possible degradation of the light source, a dual-wavelength referencing technique is used (see Fig. 3). In this fashion, two specific wavelengths are selected out of the LED's broad spectrum by narrow bandpass optical filters, and their intensities are measured using optical detectors. The magnitude of the measurand is thus related to a change in the intensity ratio at these two wavelengths.

Next, we will discuss the operation and fabrication of the FPI used in this work, along with a summary of the results obtained in its implementation as a fiber-optic electric field sensor.

ANALYSIS OF OPERATION

- *The Fabry-Perot Interferometer*

A FPI is an optical resonator cavity consisting of two, partially transmitting, parallel mirrors separated a distance d (see Fig. 4). When a collimated, monochromatic, beam of light I_0 is incident upon the cavity at an angle θ, a series of multiple reflections of the transmitted beam will take place within the cavity. Outside the cavity, a series of beams of diminishing amplitudes emerge on each side of the mirrors. These output beams interfere constructively with one another, resulting in a net reflected light intensity I_r in the direction of the light source, and a net transmitted intensity I_t, directed away from the source. The ratio of the reflected intensity *to the incident intensity can be obtained by the superposition of the fields for each beam, which results in [13]:

$$\frac{I_r}{I_0} = \frac{(\sqrt{R_1} - \sqrt{R_2})^2 + 4\sqrt{R_1 R_2}\sin^2(\frac{\delta}{2})}{(1 - \sqrt{R_1 R_2})^2 + 4\sqrt{R_1 R_2}\sin^2(\frac{\delta}{2})} \tag{1.1}$$

where R_1 and R_2 are the mirror reflectivities, and δ is the phase difference between two successive beams:

$$\delta = \frac{4\pi}{\lambda} n d \cos\theta \tag{1.2}$$

*Since our sensor design is based on the reflected intensity, we will focus our attention on I_r alone. However, a similar analysis can be made for the case of I_t.

where n is the index of refraction of the medium between the mirrors, d is the cavity spacing, θ the incidence angle, and λ the wavelength of the light in vacuum.

The behavior of $\frac{I_r}{I_0}$ as a function of phase difference δ is shown for different values of $R = \sqrt{R_1 R_2}$ in Fig. 5. The spectrum consists of a series of resonant reflection peaks that occur whenever the cavity spacing equals an integer multiple of $\frac{\lambda}{2}$ of the incident light. Hence, according to eq. 1.1, I_r will be a maximum whenever $\delta = m\frac{\pi}{2}$ with $m = 1, 2, 3, ...$, and a minimum whenever $\delta = m\pi$. The parameter m is known as the interference order and is an indication of how many fringes have occurred from a zero cavity spacing up to a spacing d. It is defined by:

$$m = \frac{\delta}{2\pi} = \frac{2nd\cos\theta}{\lambda} \tag{1.3}$$

Notice from Fig. 5 that the reflection peaks are more pronounced and narrower whenever R is large, while they become broad and almost sinusoidal in shape for small R. Furthermore, High values of R result in peaks with a greater modulation depth, as opposed to cavities with low values of R. The modulation depth or contrast c is a measure of the ratio between the maximum and the minimum reflected intensities as given below:

$$c = \frac{I_{rmax}}{I_{rmin}} = \left(\frac{1+\sqrt{R_1 R_2}}{1-\sqrt{R_1 R_2}}\right)^2 \tag{1.4}$$

The separation between peaks, $\Delta\lambda$, is known as the free spectral range (FSR) of the cavity, and is given by:

$$\Delta\lambda = \frac{\lambda^2}{2nd\cos\theta} \tag{1.5}$$

Each peak possesses a bandwidth, $\Delta\lambda_{\frac{1}{2}}$, at full width half maximum (FWHM) of:

$$\Delta\lambda_{\frac{1}{2}} = \frac{2\lambda}{\pi m}\arccos\left(\frac{1-\sqrt{R_1 R_2}}{2(R_1 R_2)^{\frac{1}{4}}}\right) \tag{1.6}$$

It is important to note that the width of the peaks depends only upon R, while their position is determined by the mirror separation d and λ. Therefore, both the spectral range and the bandwidth can be tailored independently of each other. The ratio between $\Delta\lambda$ and $\Delta\lambda_{\frac{1}{2}}$ is known as the Finesse, F, of the cavity.

Since the cavity design employs semi-reflective metallic coatings for mirrors, which inevitably absorb light, the expression for I_r is no longer accurate and has to be modified to take into account the effects of mirror absorption and the phase retardations incurred upon reflection. The modified expression for I_r has the form [14]:

$$\frac{I_r}{I_0} = \frac{(\sqrt{R_1} - g\sqrt{R_2})^2 + 4g\sqrt{R_1 R_2}\sin^2\left(\frac{\delta+\phi_2-\phi_1^R+\phi_T}{2}\right)}{(1-\sqrt{R_1 R_2})^2 + 4\sqrt{R_1 R_2}\sin^2\left(\frac{\delta+\phi_2+\phi_1^L}{2}\right)} \tag{1.7}$$

with

$$g = \left|R_1 \exp^{j(\phi_1^L+\phi_1^R)} + T_1 \exp^{2j\phi_T}\right| \tag{1.8}$$

where g is a parameter that represents the amount of light not absorbed by the front mirror (1-A); ϕ_1^R is the phase change upon reflection from the front mirror for a beam traveling away from the source; ϕ_1^L is the phase change upon reflection from mirror 1, for a beam traveling towards the source; ϕ_2 is the phase change upon reflection from the rear mirror, and ϕ_T is the phase change introduced upon crossing the first mirror. These parameters can be computed using the following expressions [13]:

$$\phi_1^R = \arctan\left(\frac{2k_{Al}\, n_{glass}}{n_{Al}^2 + k_{Al}^2 - n_{glass}^2}\right) \tag{1.9}$$

$$\phi_1^L = \arctan\left(\frac{2k_{Al}\, n_{air}}{n_{Al}^2 + k_{Al}^2 - n_{air}^2}\right) \tag{1.10}$$

$$\phi_2 = \phi_1^L \tag{1.11}$$

$$\phi_T = \phi_{glass-Al}^T + \phi_{Al-air}^T + \beta_{Al} \tag{1.12}$$

$$= \arctan\left(\frac{-k_{Al}}{n_{glass} + n_{Al}}\right) + \arctan\left(\frac{k_{Al}\, n_{air}}{n_{Al}^2 + k_{Al}^2 n_{Al} n_{air}}\right) + \frac{2\pi n_{Al} t_{Al}}{\lambda} \tag{1.13}$$

where n and k are the refractive index and extinction coefficient, respectively, for a given medium (aluminum film, glass or air). The effect of these additional phase terms is equivalent to an increase $\frac{\phi\lambda}{2\pi}$ in the optical spacing of the cavity. In addition, the maxima of the spectrum will decrease due to the absorption in the metal films.

- *Deflection of a Corrugated Diaphragm*

Since a corrugated Si diaphragm is used to transduce the measurand of interest into a mechanical deflection which subsequently will change the gap separation of the FPC, it becomes necessary to discuss the behavior of flat and corrugated diaphragms both in the linear and nonlinear regimes.

A diaphragm may be viewed as a spring element which deflects by the application of a load. The resistance to loading is due to bending, tensile forces, and pre-stresses in the diaphragm. The deflection at the center of a flat circular plate is given as [15]:

$$\frac{Pa^4}{Et^3} = \frac{16}{3(1-\nu^2)}\left(\frac{y}{t}\right) + \frac{8}{3(1-\nu^2)}\left(\frac{y}{t}\right)^3 \tag{1.14}$$

where P is the applied pressure, y the deflection, t the diaphragm thickness, a the diaphragm radius, E is Young's modulus and ν is Poisson's ratio.

Notice that Eq. 1.14 has both a linear and a nonlinear deflection terms. When the applied load is entirely supported by bending, the resulting deflection is linear. If, on the other hand, a portion of the applied load is resisted by a restoring force caused by stretching of the diaphragm, then the center deflection becomes nonlinear. The nonlinear behavior is noticeable in thin plates for which, when the deflection is larger than about half the thickness, the middle surface becomes appreciably strained giving rise to tension forces in the diaphragm. Furthermore, the deflection of flat diaphragms is not uniform across its radius, but rather the medium plane changes into the shape of a surface of revolution with characteristically defined inflection points.

In order to obtain a linear response for a greater range of deflection, a series of corrugations are incorporated on the surface of the diaphragm. A corrugated diaphragm is made by forming concentric convolutions or corrugations on the plane of a thin flat plate. The profile of the corrugations has little influence on the performance characteristics of the diaphragm and may even have different shapes such as sinusoidal, trapezoidal, triangular, rectangular or toroidal. However, the stiffness and the range of linear deflection may be altered by the depth and number of the corrugations.

In general, the introduction of corrugations increases the range of linear deflection at the expense of increasing considerably the rigidity of the diaphragm. Therefore, in order to obtain a deflection comparable to an equivalent flat diaphragm (same thickness, material and radius), an increase in the applied load will be necessary. However, if the deflection of a flat diaphragm is compared to that of a corrugated one of the same flexibility (not necessarily the same radius or thickness) the corrugated one displays a greater range of linear deflection.

The load-deflection relation for a corrugated diaphragm is given as [16]:

$$\frac{Pa^4}{E't^4} = A_p\left(\frac{y}{t}\right) + B_p\left(\frac{y}{t}\right)^3 \tag{1.15}$$

with

$$A_p = \frac{2(q+3)(q+1)}{3(1-\frac{\nu^2}{q^2})} \tag{1.16}$$

$$B_p = \frac{32}{q^2-9}\left(\frac{1}{6} - \frac{3-\nu}{(q-\nu)(q+3)}\right) \tag{1.17}$$

and for sinusoidal corrugations

$$q = \left(\frac{s}{l}\right)\sqrt{1+\frac{H^2}{t^2}} \tag{1.18}$$

where $E' = \frac{E}{(1-\nu)}$ and q is the corrugation quality factor, H the corrugation depth, s the corrugation arc length and l the spatial period (see Fig. 6). The value of q is a figure of merit that determines the deflection characteristics of the diaphragm. A high value of q implies a long range of linear displacement, as well as a high rigidity. Low values of q indicate a performance approaching that of a flat diaphragm for which $q = 1$. Furthermore, for the case of shallow corrugations, the corrugation period l has little effect since $\frac{s}{l} \approx 1$.

At times it is desirable to have a small flat region, or center boss, in the diaphragm. This is particularly useful in structures like actuators and movable mirrors (as with the present case). Small deflections of a bossed, corrugated, diaphragm were developed by Haringx [17] who expressed them as follows:

$$y = \epsilon\frac{3Pa^4}{16E't^3} \tag{1.19}$$

with

$$\epsilon = \frac{8(1-r^4)}{(q+3)(q+1)}\left(1 - \frac{8qr^4(1-r^{q-1})(1-r^{q-3})}{(q-1)(q-3)(1-r^4)(1-r^{2q})}\right)\left(\frac{s}{l}\right) \tag{1.20}$$

where r is the boss to diaphragm radius ratio (R_b/a). The parameter ϵ is known as the coefficient of reduction and physically represents the stiffening that a comparable flat diaphragm has acquired by the introduction of corrugations. In other words, the magnitude of ϵ ranges from one to zero. Hence, diaphragms with large inner rims and deep corrugations are extremely rigid. Conversely, smaller inner rims combined with shallow corrugations result in more flexible diaphragms.

Corrugated silicon diaphragms have been successfully fabricated and used in applications such as pressure sensors, micro-actuators and interferometers [18,19]. Typically, corrugations have been produced by etching grooves in the surface of a silicon wafer and then diffusing an etch-stop. The process is completed when the corrugations are defined by a deep etching on the opposite side of the wafer.

• *Dynamic Response*

The principal factors which govern the dynamic response characteristics of the sensor are the stiffness of the diaphragm, and the stiffness and damping resistance of the air-filled space inside the FPC.

When the diaphragm deflects it sets in motion the thin film of air inside the cavity. This airflow introduces forces that modify the mechanical stiffness and resistance coefficients of the cavity, which control the response of the transducer. This situation is very similar to that encountered in a condenser microphone. Therefore, the theory behind the dynamic properties of thin air films have been previously investigated to asses their impact on the performance of condenser microphones [20].

As the sensor's diaphragm moves, air is forced radially out of the cavity † resulting in a resistive force (due to the viscosity of the air) which opposes the motion of the diaphragm. In addition, there is a simple compression of the entrapped air which results in an elastic restoring force on the diaphragm. At very low frequencies, the air is able to flow out of the gap, and consequently the dominant mechanism is due to frictional forces introduced by the large airflow while the elastic forces due to air compression are negligible. Conversely, at high frequencies, there is little flow and hence larger compressive forces, while the resistive forces are minimal. The frequency-dependent magnitudes of the total damping resistance c, and stiffness k_a of the air film can be calculated from the following expressions [20]:

$$c(\omega) = \frac{2\pi a P_a}{\omega \alpha d}\left[\frac{bei(\alpha a)\ bei'(\alpha a) + ber(\alpha a)\ ber'(\alpha a)}{ber^2(\alpha a) + bei^2(\alpha a)}\right] \tag{1.21}$$

$$k_a(\omega) = \frac{\pi a^2 P_a}{d}\left[1 - \frac{2}{\alpha a}\frac{ber(\alpha a)\ bei'(\alpha a) - ber'(\alpha a)\ bei(\alpha a)}{ber^2(\alpha a) + bei^2(\alpha a)}\right] \tag{1.22}$$

with

$$\alpha = \frac{12\nu\omega}{P_a d^2} \tag{1.23}$$

where P_a is the atmospheric pressure, a is the radius of the diaphragm, d the cavity spacing, and ν the air viscosity. As before, for frequencies near zero K_a vanishes, while c simplifies to the following:

$$c = \frac{3}{2}\frac{\pi \nu a^2}{d^3} \tag{1.24}$$

The actual response of the sensor is obtained by modeling it as a second-order system with frequency-dependent damping and stiffness. In this fashion, when a force $F\cos(\omega t)$ acts on the diaphragm, the resulting displacement can be determined from the equation of motion for the system that is,

$$m\ddot{x} + c\dot{x} + (k_a + k_d) = F\cos(\omega t) \tag{1.25}$$

where k_d is the stiffness of the diaphragm. The net displacement amplitude X can be obtained by solving Eq. 2.95, obtaining the following expression [21]:

$$X = \frac{F}{\{(k_a + k_d) - m\omega^2\} + \jmath c\omega} \tag{1.26}$$

† This airflow is free to escape the cavity through a series of minute vent holes provided on the rim area of the diaphragm. The vent holes are also used to maintain the cavity at atmospheric pressure, thus avoiding any pressure differentials from introducing any errors on the measurements, except in the case of a pressure transducer where their use might be precluded.

Under static conditions ($\omega = 0$), k_a is negligible and, although the airflow damping resistance c might reach high values, its actual contribution to the system as a whole is zero, so that the static deflection simply becomes

$$X_{st} = \frac{F}{k_d} \tag{1.27}$$

At high frequencies the response of the system is highly dependent on the air's damping and stiffness effects. The detrimental influence of these effects can be minimized by facilitating the flow of the entrapped air film by means of holes or deep channels on the surface of the cavity substrate.

Another important aspect of the dynamic response behavior of this system, is its temporal transient response which describes how the system reacts to and follows a unit-step input. The unit-step response $x(t)$ for this system has the form:

$$x(t) = 1 - \frac{\exp(-\zeta\omega_n t)}{\sqrt{1-\zeta^2}} \sin\left(\omega_d t + \arctan\frac{\sqrt{1-\zeta^2}}{\zeta}\right) \tag{1.28}$$

where

ω_n = natural frequency of the system $\left(\sqrt{\frac{k_d}{m}}\right)$

ω_d = damped natural frequency of the system ($\omega_n\sqrt{1-\zeta^2}$)

ζ = damping ratio $\left(\frac{c(\omega)}{c_{cr}} = \frac{c(\omega)}{2m\omega_n}\right)$

Eq. 1.28 above indicates that the transient step-response of this type of system consists of either free or damped oscillations at a frequency ω_d. That is, if $\zeta = 0$, the system oscillates at its natural frequency ω_n. However, if the linear system has any amount of damping, the oscillations occur a a much lower frequency than ω_n, decaying exponentially in time. For the case of an overdamped system ($\zeta > 1$), the oscillations are non-existing and the response of the system varies exponentially with time. The time required for the output response to reach and stay within a given range of the initial value is known as the settling time τ_s. For overdamped systems, $\tau_s \approx \frac{6}{\zeta\omega_n}$ for a 2% tolerance band.

FABRICATION

A wide variety of corrugated Si diaphragms having different radii, boss-ratio, thickness and number of vent holes, were fabricated using standard photolithographic and silicon micromachining techniques [22-24]. Next, we will describe the fabrication process in more detail.

First, a small circular recess $1.7\mu m$ deep is etched on the epi side of a n-type, (100) Si wafer, using a solution of KOH:DI:IPA (900gm:900ml:360ml) at 80^0C for 2.5 minutes (see Fig. 7a). Subsequently, a series of concentric grooves, $5\mu m$ deep, are plasma-etched using a gas mixture of $CF_4 : O_2$ (10:1) at a pressure of approximately $400mT$ and $300W$ of power. These grooves will define the top side of the corrugations (see Fig. 7b).

A thick ($1.2\mu m$) thermal oxide layer is grown on the wafer to mask against the boron diffusion and to allow the patterning of the backside for the deep anisotropic etching. This oxide mask is photolithographically patterned to define circles of $100\mu m$ in diameter around the periphery of the recess. These oxide dots will block the subsequent boron diffusion, thus allowing the etch to attack the silicon all the way through in these regions. At this point, a heavy boron diffusion is introduced at a temperature of 1175^0C to act as an etch-stop. The diffusion time varied from 25 minutes (for a $3\mu m$ thickness), to 33 minutes ($3.5\mu m$), up to 1 hour ($5\mu m$). After the boron diffusion, the wafers are briefly etched in a solution of HF:DI (1:1) to remove the borosilicate glass that developed from the diffusion (see Fig. 7c).

To complete the processing, a deep etching on the backside of the wafer is made using an EDP solution (ethylenediamine, pyrocatechol and water) at 110^0C for 5 hours. Since the boron diffusion follows the contour of the epitaxial features on the wafer, a thin, corrugated, Si diaphragm with a thickness dependent on the depth of the boron diffusion will be obtained after the backside etching is completed (see Fig. 7d). Finally, the wafers are thoroughly rinsed and the remaining oxide layer removed in buffered HF.

The final aspect of the diaphragms can be appreciated in Fig. 8, which shows SEM photographs of different versions of corrugated diaphragms, including one with a central mesa. Notice how well defined the structural features are, as well as the smooth shiny finish of the silicon. The diaphragms appear translucent with an orange-red color. They are also straight and taut due to the heavy boron doping and, for the most part, they seem relatively rugged. However, they easily shatter or break if punctured or touched abruptly.

The FPC were formed by bonding together a mirrored diaphragm with a metallized pyrex substrate. For this application, $1cm$ square pyrex microscope cover slips, $300\mu m$ thick and polished flat to $5\lambda/in$, covered with a thin ($60\mathring{A}$), partially transmitting film, were used. Cavities were permanently bonded using the anodic bonding technique [25]. The bonded FPC were mounted on the tip of a multimode fiber ($100/140\mu m$) where a GRIN lens was previously attached to, as depicted in Fig. 2.

EXPERIMENTAL RESULTS

The reflected intensity spectra for assembled FPI was measured using an arrangement similar to the one depicted in Fig. 3. Light from a white-light source was launched into one arm of a fused fiber coupler connected to the fiber probe, and the reflected light from the cavity is measured through the opposite arm of the fiber coupler by means of an optical spectrum analyzer. Fig. 9a shows a typical spectrum in the 600 to $1100nm$ range for an undeflected FPC with a $5\mu m$ gap and $R_1 = 0.2$ and $R_2 = 0.8$. The spectrum is characterized by smooth and well defined interference cycles. However, there is a broadening effect that results in "rounder" aspect of the minima regions, which is not characteristic of typical FPC spectra. This effect is a consequence of the phase changes introduced by the metallic films upon reflection that modify the characteristics of the reflected intensity as confirmed by the calculated reflection spectrum shown in Fig. 9b. Obtained using Eq. 1.7 and the same cavity parameters.

Another important aspect observed in the course of these measurements, was the sensitivity of the alignment between the FPC and the GRIN lens. It was noticed that in some instances optical interference was not observed for the cavity when a GRIN lens was used. This can be attributed to either a "run-away" effect in the cavity (where the multiple reflected beams do not interfere properly with one another because of spatial shifts introduced by skews rays), or by improper re-launching of the light back into the fiber due to a fiber misalignment with respect to the GRIN lens, or perhaps due to lack of parallelism between the mirrors over the area of the GRIN lens ($1.8mm$ in diameter). This latter explanation seems to be a plausible one, since in experiments relying exclusively on the coupling between the multimode fiber and the cavity, interference was observed with an adequate amount of reflected intensity.

To demonstrate the proof-of-principle of the FPC, a novel electric field sensor was constructed using a combination of a Faraday cage and the miniature FPI described here. By constructing the FPC as a conductive Faraday cage, external electric fields can be detected by the electrostatic forces they exert on the top surface of the cavity's diaphragm. Thus, as the gap in the cavity increases, under the influence of the negative electrostatic pressure induced by the external field, the intensity of the backreflected light into the fiber will change accordingly (consult reference [26] for more details on the operation of this sensor).

Measurements of reflected spectra were made with a probe placed inside and electric-field test cage consisting of two parallel metallic plates separated by dielectric rods and connected to the terminals of a variable $30KV$ DC power supply.

Reflected intensity spectra, for different intensities of applied electric field, were obtained using an LED emitting at $850nm$ as a source. Measured spectra at different applied field intensities are shown in Fig. 10. Notice that the cavity's diaphragm does indeed deflect under the influence of the external field and that this deflection brings upon a change in the reflected spectrum of the LED. Furthermore, $40KV/m$ was the minimum field for which a deflection was observed. This is attributed to the residual stress present in the diaphragm due to the heavy boron-doping used in its fabrication. Diaphragms fabricated using a stress-free process such as the electrochemical etching process, will result in sensors with increased sensitivity.

CONCLUSIONS

A new design for a miniature FPI mounted on an optical fiber for sensing applications has been demonstrated. The present device combines optical fibers with silicon micromachining techniques to render a new family of fiber optic sensors that offer small size, lightweight, EMI immunity as well as high sensitivity for the detection of a variety of measurands.

The optical and mechanical characteristics of the FPI have been analyzed in some detail, and their potential application demonstrated in the form of an electric field sensor. DC electric fields in the range of 0 to $300KV/m$ have been successfully measured. The minimum field strength detected was of the order of $40KV/m$. This relatively low sensitivity is due to the high stiffness of the diaphragm arising from the high boron-diffusion. However, higher sensitivities are possible by thinning the diaphragm, increasing the radius, reducing the boss ratio or decreasing the corrugation depth.

ACKNOWLEDGEMENT

The authors wish to thank S. Cho for helpful discussions on silicon micromachining.

REFERENCES

1. Guckel, H. et al., "Electromechanical Devices Utilizing Thin Si Diaphragms", Appl. Phys. Lett., Vol. 31, No. 9, pp. 618-619, 1977.

2. Jerman, J. H. and Mallinson, S. R., "A Miniature Fabry-Perot Interferometer Fabricated Using Silicon Micromachining Techniques", Technical Digest of the 1988 IEEE Solid-State Sensors Workshop.

3. Jerman, J. H., Clift, D. J. and Mallinson, S. R., "A Miniature Fabry-Perot Interferometer with a Corrugated Silicon Diaphragm Support", Sen. Act., Vol. A 29, pp. 151-158, 1991.

4. Halg, B., "A Silicon Pressure Sensor with an Interferometric Optical Readout", Proc. Transducers '91 Conf., San Francisco, CA, June 1991, pp. 682-684.

5. Raley, N. F., Ciarlo, D. R., Koo, J., Beiriger, B., Trujillo, J., Yu, C., Loomis, G., and Chow, R., "A Fabry-Perot Microinterferometer for Visible Wavelengths", Technical Digest of the 1992 IEEE Solid-State Sensor and Actuator Workshop, June 1992, Hilton Head, SC.

6. Cox, E. R. and Jones, B. E., "Fibre Optic Colour Sensors Based on Fabry-Perot Interferometry", Proc. First International Conference on Optical Fiber Sensors, London, England, 1983.

7. Lieberman, R. A. and Blonder, G. E., "An Improved Interferometric Pressure Optrode", SPIE Proc., Vol. 838, pp. 49-59, 1987.

8. Dakin, J. P., Wade, C. A. and Withers, P. B., "An Optical Fibre Sensor for the Measurement of Pressure", Fiber and Int. Opt., Vol. 7, pp. 35-40, 1988.

9. Wolthuis, R. A., Mitchell, G. L., Saaski, E., Hartl, J. C. and Afromowitz, M. A., "Development of Medical Pressure and Temperature Sensors Employing Optical Spectrum Modulation", IEEE Trans. Bio. Eng., Vol. 38, No. 10, pp. 974-981, 1991.

10. Beheim, G., Fristch, K., Tabib Azar, M., "Silicon-Etalon Fiber-Optic Temperature Sensor", SPIE Proc., Vol. 1169, pp. 504-511, 1989.

11. Saaski, E. W., Mitchell, G. L., Hartl, J. C., "Wide Range Sensing of Liquid Refractive Index", Proc. Optical Fiber Sensors '86 conf., paper FAA 5-1, pp. 361-364, 1988.

12. Mitchell, G. L., "A Review of Fabry-Perot Interferometric Sensors", Springer Verlag proceedings in Physics, Vol. 44, Optical Fiber Sensors, pp. 450-457, 1989.

13. Born, M. and Wolf, E., Principles of Optics, Pergamon Press, New York, 1984.

14. Hadley, L. N., and Dennison, D. M., "Reflection and Transmission Interference Filters", J. Opt. Soc. Am., Vol. 37, No. 6, pp. 451-465, 1947.

15. Timoshenko, S. and Woinowsky-Krieger, S., Theory of Plates and Shells, McGraw Hill, New York, 1959.

16. DiGiovanni, M., *Flat and Corrugated Diaphragm Design Handbook*, Marcel Dekker, Chapter 23, 1982.

17. Haringx, J. A., "The Rigidity of Corrugated Diaphragms", Appl. Sci. Res., Vol. A2, pp. 299-325, 1950.

18. Mallon, J. R. and Kurtz, A. D., "Transducer Apparatus Employing Convoluted Semiconductor Diaphragms", U.S. Patent 4,467,656, 1984.

19. Jerman, J. H., "The Fabrication and Use of Micromachined Corrugated Silicon Diaphragms", Sens. Act., A21-A23, pp. 988-992, 1990.

20. Crandall, I. B., "The Air-Damped Vibrating System: Theoretical Calibration of the Condenser Transmitter", Phys. Rev., Vol. 11, pp. 449-460, 1918.

21. Rule, E., Suellentrop, J. and Perls, T. A., "Second-Order Instrumentation Systems with Frequency-Dependent Stiffness and Damping", J. Acoust. Soc. Am., Vol. 31, pp. 457-462, 1959.

22. Petersen, K. E., "Silicon as a Mechanical Material", Proc. IEEE, Vol. 70, No. 5, pp. 420-457, 1982.

23. Delapierre, G., "Micro-Machining: A Survey of the Most Commonly Used Processes", Sens. Act., Vol. 17, pp. 123-138, 1989.

24. Bassous, E., "Fabrication of Novel Three-Dimensional Microstructures by the Anisotropic Etching of (100) and (110) Silicon", IEEE Trans. Elect. Dev., Vol. ED-25, No. 10, pp. 1178-1185, 1978.

25. Wallis, G. and Pomerantz, D. I., "Field Assisted Glass-Metal Sealing", J. Appl. Phys., Vol. 40, No. 10, pp. 3946-3949, 1969.

26. Méndez, A., Morse, T. F. and Ramsey, K., "Fiber Optic Electric-Field Microsensor", Proc. SPIE, Vol. 1795, No. 17, Fiber Optic and Laser Sensors X, Boston, MA, 1992.

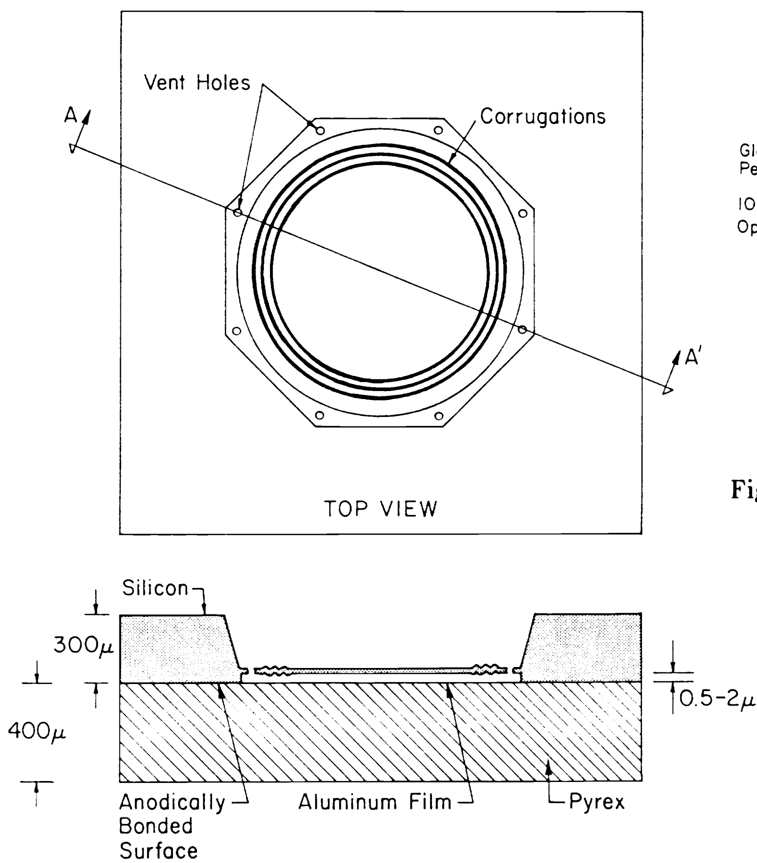

Figure 1: Fabry-Perot microcavity

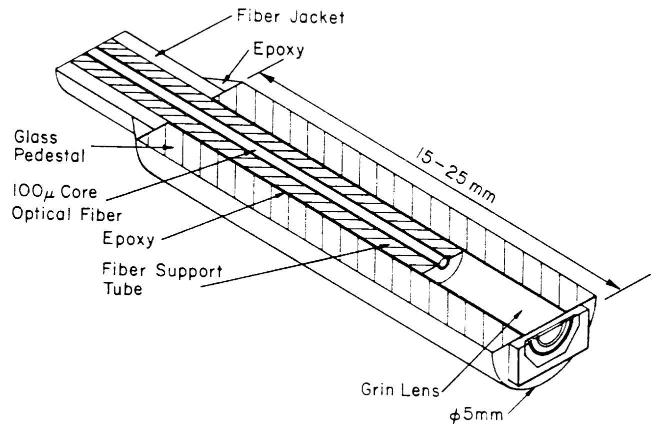

Figure 2: Mounting of sensor cavity on an optical fiber

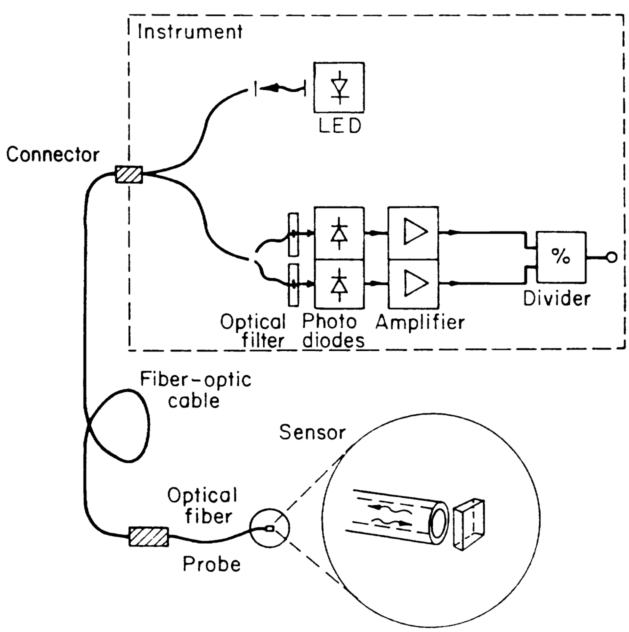

Figure 3: Sensor system schematic

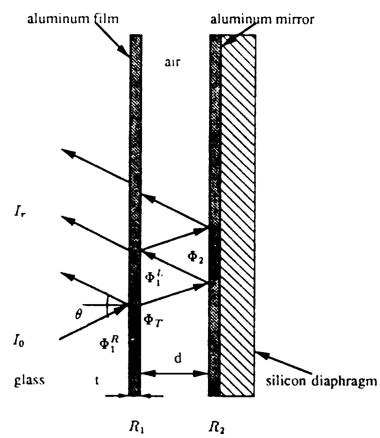

Figure 4: Fabry-Perot interferometer

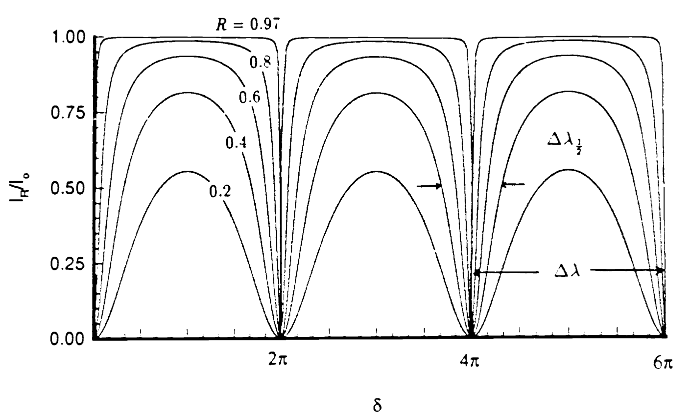

Figure 5: Fabry-Perot cavity reflected spectrum

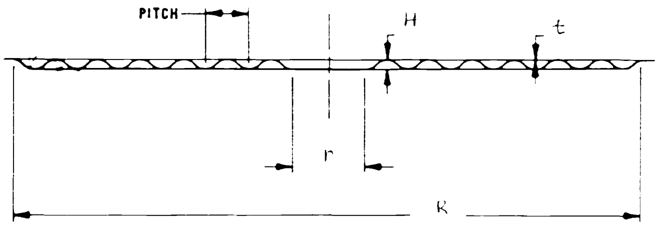

Figure 6: Profile of a corrugated diaphragm

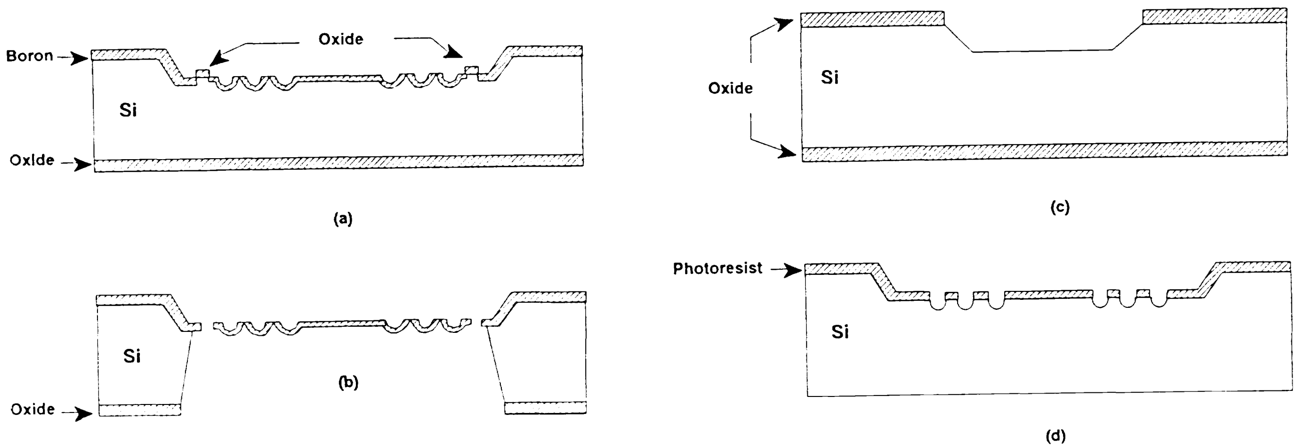

Figure 7: Micromachined corrugated silicon diaphragm fabrication process

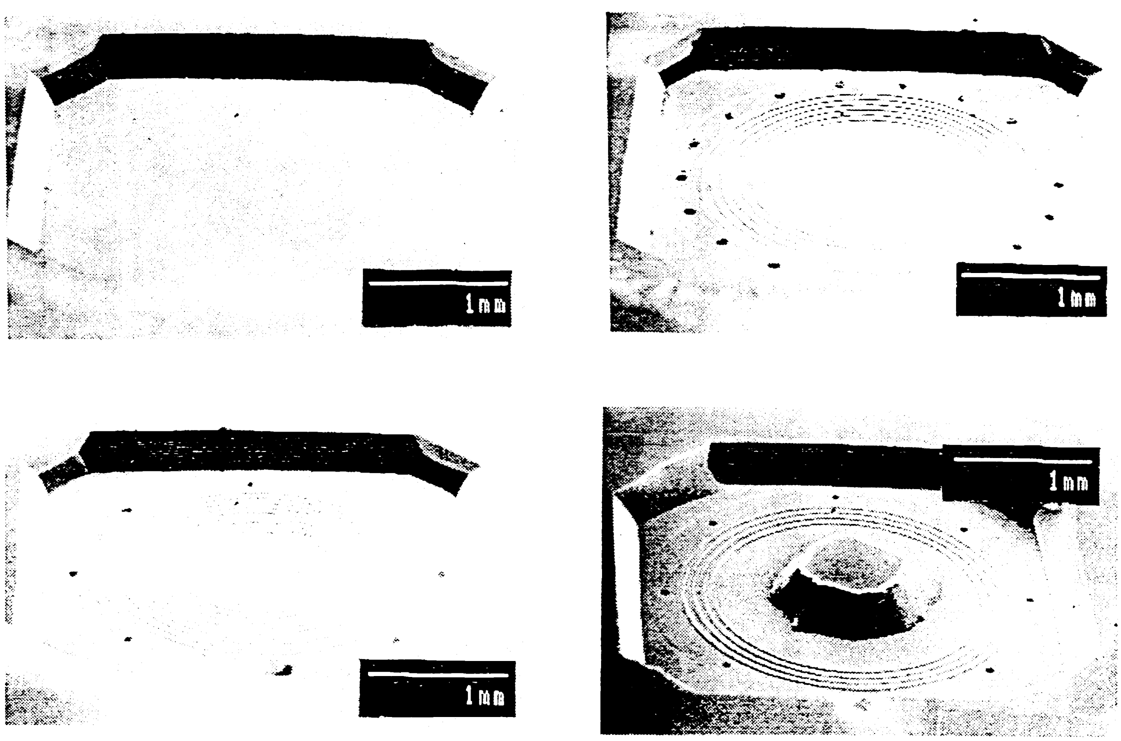

Figure 8: SEM photographs of various micromachined silicon diaphragms

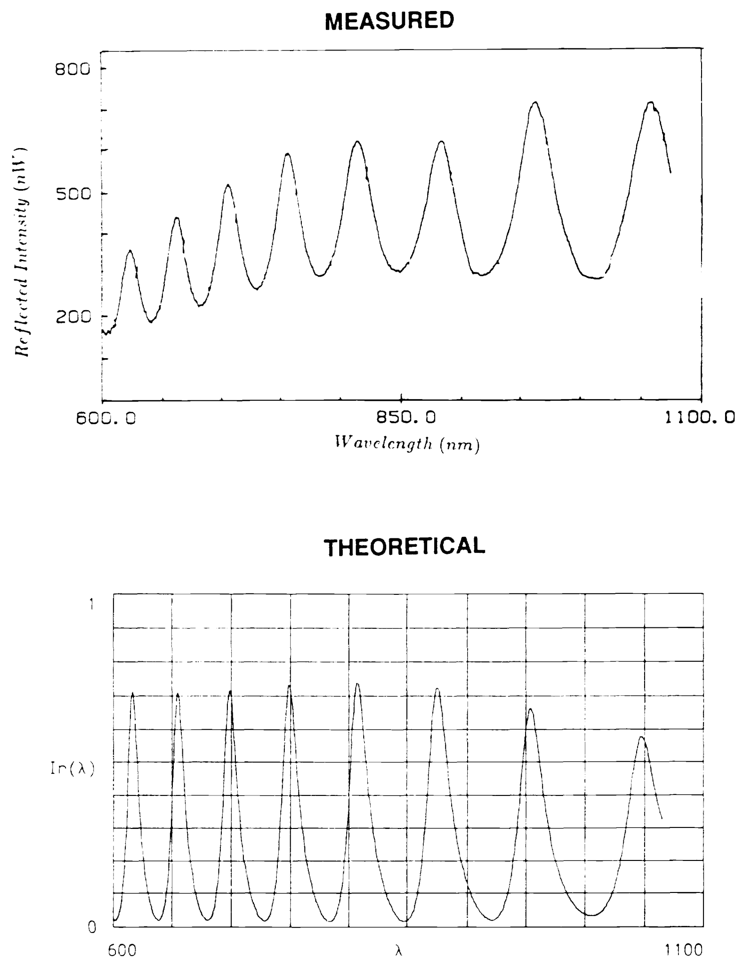

Figure 9: a) Measured FPC reflected spectrum and b) Calculated reflected spectrum using Eq. 1.7

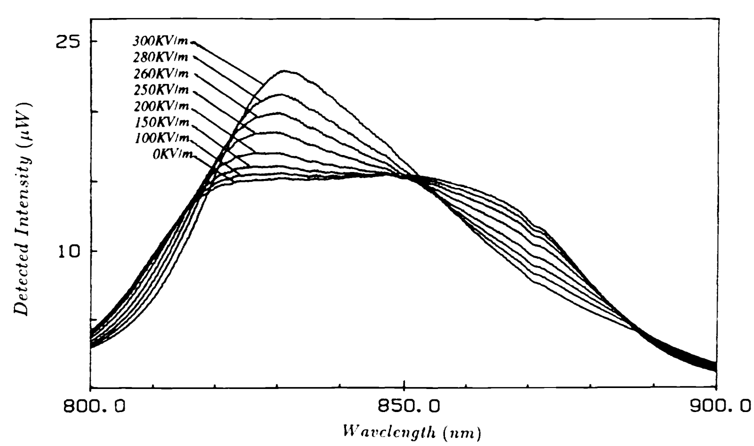

Figure 10: Measured reflected spectra for different intensities of electric field.